Bandgap Tuning of Silicon Micromachined 1-D Photonic Crystals by Thermal Oxidation

Giuseppe Barillaro, Sabina Merlo, *Senior Member, IEEE*, and Lucanos Marsilio Strambini

***Abstract*—Fabrication and optical testing of high-aspect-ratio 1-D photonic crystals, obtained by electrochemical micromachining of silicon, are discussed in this paper. The devices consist of high-aspect-ratio periodic ($P = 4$ μm) arrays of 1.22-μm-thick silicon walls separated by 2.78-μm-wide air gaps, with 100 μm etching depth. They were designed as hybrid quarter-wavelength reflectors with photonic bandgaps in the near-IR region, one in particular centered at $\lambda = 1.55$ μm. The fabrication process was improved to increase structure uniformity and strength. Thermal oxidation of the silicon structures was exploited to tune the wavelength position and width of the bandgaps. Fabricated devices, also with different silicon dioxide thicknesses, were optically tested by measuring their spectral reflectivity in the wavelength range of 1.0–1.7 μm. Experimental results were found in good agreement with the calculated spectra.**

***Index Terms*—Micromachining, optical components, optical device fabrication, optical reflection, photonic bandgap materials, silicon.**

I. Introduction

SILICON photonics involves scientific researches devoted to the design and fabrication of optical components, by applying inexpensive, well-developed manufacturing processes to high-quality silicon wafers, easily available at relatively low cost (when compared in particular to other optical materials). A traditional motivation for justifying researches on silicon photonics still remains the fabrication of optical devices in high volume at lower costs, with the additional advantages offered by the unique material properties of silicon [1], [2]. Although wideband optical communication networks have been the initial driving market for silicon photonics, other fields may obtain benefits from its development.

Besides optical components with classical functions, photonic bandgap materials and devices with new features represent a growing research area in the field of silicon photonics. Photonic bandgaps within selected wavelength regions have been theoretically predicted and experimentally observed in 1-D periodic structures fabricated with dielectric materials [3], [4]. In particular, high-order propagation gaps in the wavelength range of 1.0–1.7 μm have been both theoretically and experimentally detected in periodic 1-D vertical microstructures, with high aspect ratio (up to 100), fabricated by the electrochemical etching of a prepatterned (1 0 0) silicon substrate [5], [6]. Other examples of high-aspect-ratio optical structures based on different technological processes and materials have also been reported in literature [7]–[9].

Among microoptoelectromechanical systems (MOEMS), micromachined mirrors and optical components are often characterized by lateral sizes of the order of hundreds of micrometers. The critical issue of obtaining large-area vertical reflecting devices starting from planar microstructures can be overcome by a direct fabrication of vertical devices by electrochemical micromachining (ECM). These recently demonstrated devices are based on the so-called hybrid quarter-wavelength structure [5] and consist in periodic arrays of silicon layers with thickness d_{Si} and air gaps of width d_{air}, which must satisfy the conditions $d_{\mathrm{Si}} = N\lambda/4\mathrm{n}_{\mathrm{Si}}$ and $d_{\mathrm{air}} = M\lambda/4$, where *N* and *M* are odd integer, independent parameters, n_{Si} is the silicon refractive index at λ (whereas air refractive index is 1), and λ is the wavelength around which a propagation gap (of higher order) is desired. This approach for realizing 1-D photonic crystals (1-D-PCs) makes it possible to select the values of silicon thickness and air gap width yielding the minimum period, but at the same time, satisfying the constraints imposed by the lithography and the technological process, as well as ensuring mechanical reliability and stability. Vertical structures, based on silicon walls with a 1–2 μm thickness, 3–4 μm pitch, and 100 μm etching depth, obtained by the ECM, can be envisioned as building blocks of optical devices, such as reflectors and optical filters, working in the near-IR wavelength region.

ECM [10]–[12] is a new, recently proposed technique for silicon microstructuring that is an alternative to other standard micromachining methods reported in literature. It is based on the electrochemical etching of an n-type silicon substrate in a solution based on hydrofluoric acid (HF) under anodic polarization and backside illumination. This well-known technique, used for regular macropore formation for over a decade [13]–[15], only recently has been demonstrated to be a powerful method for the fabrication of a number of silicon microstructures, such as squared and circular spirals, tubes and pillars, and walls, with applications for microelectronics [16], space [17], optics [5], [6], and microfluidics [18].

In this paper, ECM was exploited for the fabrication of high-aspect-ratio silicon–air 1-D-PCs, according to the fabrication process reported in Section II. With respect to previously published papers, the process was optimized to obtain a more uniform air gap width throughout the entire etching

Manuscript received November 30, 2007; revised January 4, 2008. This work was supported in part by the European Union (EU) Project PICASSO IST-2005-34551.

G. Barillaro and L. M. Strambini are with the Dipartimento di Ingegneria dell'Informazione: Elettronica, Informatica, Telecomunicazioni, Università di Pisa, 56126 Pisa, Italy (e-mail: g.barillaro@iet.unipi.it; lucanos.strambini@iet.unipi.it).

S. Merlo is with the Dipartimento di Elettronica, Università degli Studi di Pavia, 27100 Pavia, Italy (e-mail: sabina.merlo@unipv.it).

Color versions of one or more of the figures in this paper are available online at http://ieeexplore.ieee.org.

Digital Object Identifier 10.1109/JSTQE.2008.916183

1077-260X/$25.00 © 2008 IEEE

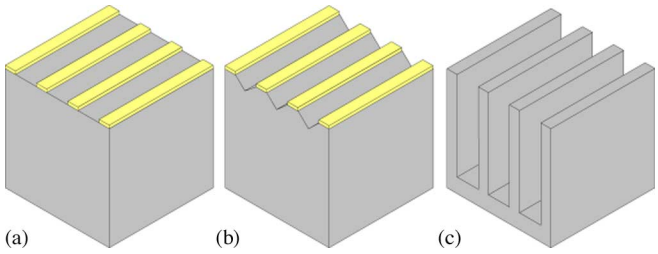

Fig. 1. Schematic fabrication process of hybrid silicon–air 1-D-PCs by means of ECM. (a) After the photolithographic step and BHF etch for pattern definition. (b) After the KOH etching step for seed formation. (c) After the electrochemical etching for trenches formation.

depth. Moreover, some technological steps in the micromachining were added to reduce stiction problems in the drying phase. In order to tune the wavelength position and the width of the bandgaps, we exploited thermal oxidation of the micromachined structures. In Section III, absolute values of reflectivity at selected wavelengths around 1.55 μm are reported to highlight the good optical properties of the bandgap material in terms of intrinsic losses in reflection. We also show the results of experimental measurements of spectral reflectivity, performed with a fiber-optic setup, on various samples of 1-D hybrid quarter-wavelength silicon microstructures, also with different oxide thicknesses. Experimental data are in good agreement with calculated spectra, also reported in the figures, and show the actual possibility of tuning the 1-D-PC bandgap by means of thermal oxidation.

II. Fabrication of 1-D-PCs by Electrochemical Micromachining

The fabrication of 1-D-PCs is based on the ECM (Fig. 1) that is characterized by the following main features:

1) high flexibility of the shape and size of the feasible structures [11], [12], [17], [18];
2) independence of the etching from crystalline directions of the substrate after (1 0 0)-oriented silicon substrates are given [12];
3) the possibility of changing the porosity D (defined as $D = \mathrm{Vol_{etch}}/\mathrm{Vol_{tot}}$, where $\mathrm{Vol_{etch}}$ is the etched silicon volume and $\mathrm{Vol_{tot}}$ is the total silicon volume under etching), and in turn, the dimension of the structure under fabrication during the etching process [15], [18];
4) independent control of lateral (through etching current) and vertical (through etching time) dimensions [18];
5) a maximum etching depth up to wafer thickness after a proper etching time is chosen [15];
6) high aspect ratio (over 250) and high integration density [5], [14], [17];
7) high lateral and vertical uniformity over large areas, as a consequence of the negative feedback due to the etching method [19];
8) good reproducibility after the etching parameters are chosen.

The ECM thus combines the advantages of both dry [e.g., reactive ion etching (RIE)] and wet [e.g., heated potassium hydroxide (KOH), tetra-methyl ammonium hydroxide (TMAH), HF–nitric acid–acetic acid (HNA)] standard silicon etchings. In fact, the ECM represents a unique case of straightforward, low-cost wet etching with the microfabrication flexibility typical of complex, very expensive dry-etching processes.

The ECM process, investigated for the fabrication of high-aspect-ratio silicon–air 1-D-PCs, is shown schematically in Fig. 1. Design parameters at $\lambda = 1.55$ μm were $n_{\mathrm{Si}} = 3.48$, $d_{\mathrm{Si}} = 1.22$ μm, and $d_{\mathrm{air}} = 2.78$ μm, corresponding to $N = 11$ and $M = 7$. The starting material was a 550-μm-thick n-doped silicon wafer, (1 0 0)-oriented, with a 3–8 Ω·cm resistivity, and with a 100-nm-thick thermally grown silicon dioxide layer on its top. Three arrays of 2-mm-long parallel straight lines, with a width of 2 μm and a pitch of 4 μm, were defined on the sample by means of a standard lithographic step. A buffered HF (BHF) etch followed by a KOH etch were used to transfer the pattern in the silicon dioxide and the silicon substrate, respectively. The KOH etch formed full V-grooves as initial seeds for the following step. Electrochemical etching in an HF-based solution was then used to fabricate deep regular trenches in the patterned substrate. The KOH etch strongly depends on crystalline directions of silicon so that its use to form seeds is limited to certain wafer orientations. To overcome this constraint, silicon isotropic etching, such as HNA, can be used for the seed formation [12].

The experimental setup used for the electrochemical silicon etching consisted of a polytetrafluoroethylene (PTFE) electrochemical cell. The electrolyte composition was 5% HF(vol):95% $\mathrm{H_2O}$(vol), with 1000 ppm (0.1%) of surfactant (Sodium Lauryl Sulfate, SLS) as a wetting agent. Backside illumination of the sample was performed with a 250 W halogen lamp through a circular window in the metal electrode that was used to provide the electrical contact to the silicon substrate. A feedback loop allowed the lamp power and, thus, the illumination power, to be changed in order to set the etching photocurrent. An IR blocking filter with a cutoff wavelength of 750 nm was placed between the sample and the lamp in order to avoid the thermal carrier generation. A second feedback loop allowed the working temperature to be set at a given value during the entire experiment. The cathode was a platinum disc put a few centimeters away from the silicon, while a platinum wire close to the sample surface (about 5 mm) was used as a reference electrode. A source meter unit was used to apply the anodization voltage V_{etch} between the silicon sample and the reference electrode and to monitor the etching current I_{etch} between the silicon sample and the cathode.

A preliminary study was carried out to find the working region for the ECM by analyzing the *I–V* curve of the Si–HF electrochemical system under investigation at the working temperature of 22 °C, according to [11] and [14]. In fact, after the characteristic current peak I_{ps}, at V_{ps}, of the *I–V* curve is given, the ECM working region is restricted to $V_{\mathrm{etch}} > V_{\mathrm{ps}}$ and $I_{\mathrm{etch}} < I_{\mathrm{ps}}$. The typical *I–V* curve of the Si–HF system under investigation, obtained by averaging different measurements at 22 °C, is reported in Fig. 2, along with the ECM working region. The *I–V* curve shows a current peak $I_{\mathrm{ps}} = 48.13$ mA at $V_{\mathrm{ps}} = 1.3$ V, and in turn, an ECM working region for $V_{\mathrm{etch}} > 1.3$ V and $I_{\mathrm{etch}} < 48.13$ mA. It is important to note that once the V_{etch}

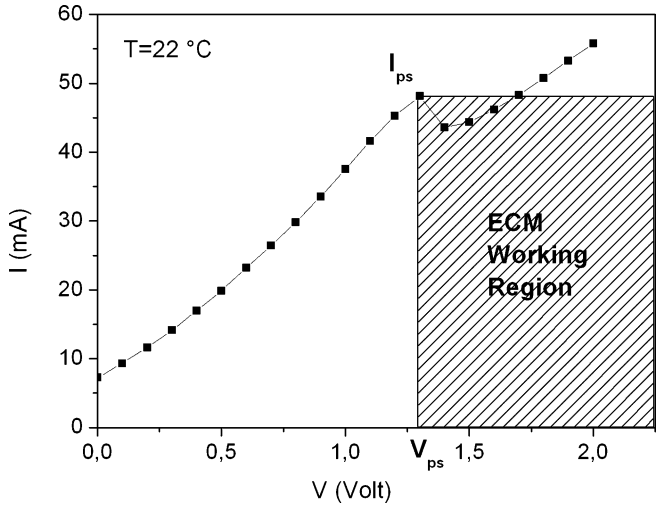

Fig. 2. Typical *I–V* curve and relative ECM working region for an n-type silicon substrate immersed in an HF-based electrolyte with HF concentration of 5%.

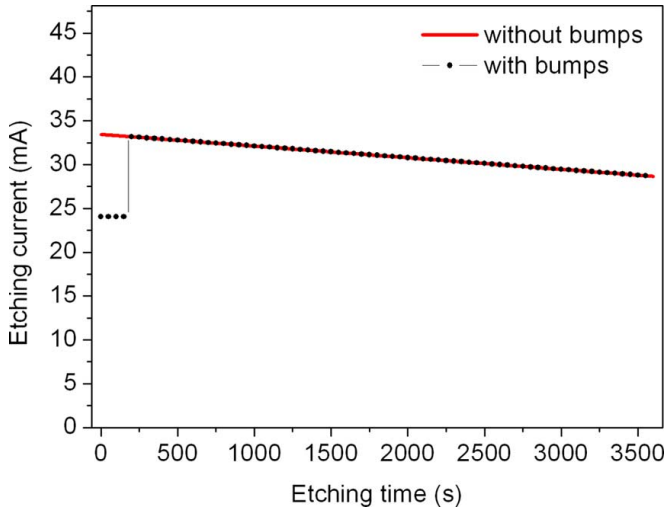

Fig. 3. Time evolution of the optimized etching current employed to etch 100-μm-deep trenches with a constant porosity $D = 69.5\%$, without bumps (solid line, red online) and with bumps (dotted line), reducing the porosity to $D = 50\%$ at the top of the structure.

is set to a value higher than $V_{\rm ps}$, the porosity D of the etched structure depends on the etching current according to the relation $D = I_{\rm etch}/I_{\rm ps}$ [15], [18].

The etching voltage $V_{\rm etch}$ was thus set to a constant value of 2 V for the entire etching process. On the other hand, the etching current $I_{\rm etch}$ was set to an initial value $I_{\rm etch0} = 33.45$ mA and reduced during the etching time according to the following relation between current and time t: $I_{\rm etch}(t) = I_{\rm etch0} - kt$, where $k = 1.328 \times 10^{-3}$ mA/s, in order to get a constant porosity value of 69.5% throughout the entire etching depth. This porosity value corresponds to silicon walls of 1.22 μm separated by 2.78-μm-thick air gaps, according to the 1-D-PC design specifications. In fact, for a specified temperature, the limit current $I_{\rm ps}$ depends on the HF concentration according to the following equation: $I_{\rm ps} = aC_{\rm HF}^{b}$, where $C_{\rm HF}$ is the actual HF concentration, a is a proper constant, and $b = 1.5$ [20]. As etching progresses, the HF concentration within the trenches decreases nonlinearly from the bulk value $C_{\rm HF0} = 5\%$, corresponding to the measured $I_{\rm ps}$ value reported in Fig. 2, and tends toward an asymptotic value of $C_{\rm HF1} < C_{\rm HF0}$ for a very long etching depth [20]. As a consequence of the HF concentration reduction within the etched trenches, the $I_{\rm ps}$ value at a given depth also reduces. In order to get constant porosity along the depth, it is then necessary to change the etching current value according to the $I_{\rm ps}$ variation. For a limited etching depth, it is theoretically feasible to approximate the nonlinear relationship between the electropolishing current and the etching time with a linear behaviour, according to the following relationship $I_{\rm ps}(t) = I_{\rm ps} - k{\cdot}t$, at least for trenches as deep as 100 μm. As a consequence, the etching current was varied during the etching process with the linear behaviour $I_{\rm etch}(t)$ already reported. The etching current was thus decreased during the etching process, from $I_{\rm etch0}$ to the final value $I_{\rm etch1} = 28.67$ mA at $t = 3600$ s, as shown in Fig. 3 (solid line). The etching time value was chosen to fully etch 100-μm-deep trenches.

After the electrochemical etching, a drying step aimed at the evaporation of the liquid filling the trenches is required. Because the length of the fabricated silicon walls (2 mm) is much greater than both the thickness (1.22 μm) and the height (about 100 μm), each wall can be modeled as a cantilever beam having a length of 100 μm and a thickness of 1.22 μm, clamped at the bottom and free at the top, at least far away from the edges. During the evaporation phase, the surface tension of the liquid–air interface gives rise to a net attractive force between two adjacent silicon walls, according to the following equation: $F = (2A\gamma_{\rm la}\cos\theta_{\rm c})/d$, where A is the solid–liquid contact area, $\gamma_{\rm la}$ is the surface tension of the liquid–air interface, $\theta_{\rm c}$ is the contact angle, and $d = d_{\rm air}/2$ is half of the distance $d_{\rm air}$ between adjacent walls [21]. The capillary force F elastically deforms the free top part of the silicon planes until they come into contact, giving rise to stiction. After the geometric characteristics of the 1-D-PC are given, according to design specifications, one way to reduce stiction problems would be to exploit low-surface-tension liquids to diminish the surface tension $\gamma_{\rm la}$ at the liquid–air interface, and in turn, the attractive force between adjacent planes. Therefore, after the electrochemical etching step, the samples were rinsed for 600 s with a cleaning solution composed of 1:4 = HF (48%):C_2H_5OH (99.99%) (vol) to remove surfactant from inside the trenches, and they were washed with ethanol and pentane in order to reduce stiction problems during the next drying step performed on a hotplate set at 180 °C for few seconds. A typical result is reported in Fig. 4, which shows an SEM cross section of a 1-D-PC about 100 μm deep and two magnifications of the upper and bottom part of the structure. The figure shows high uniformity for both the horizontal and vertical directions of the etched structure, which is indispensable for the fabrication of reliable 1-D-PCs. Statistical measurements on SEM images of 1-D-PCs with different period, porosity, and etching depth yielded for the width of the silicon walls a standard deviation of a few nanometers along the horizontal axis (through the whole sample) with respect to the mean value, and a relative error of the order of 1% along the vertical direction (between the top and the bottom of the

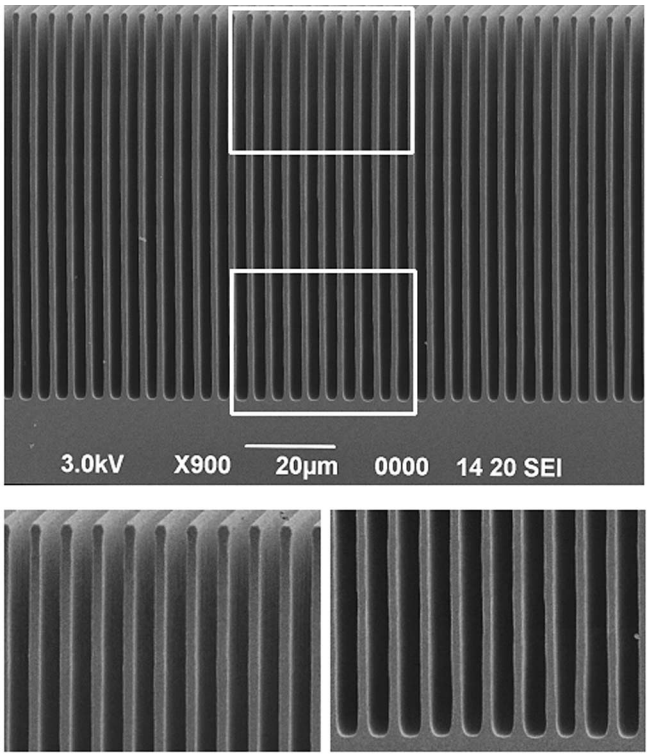

Fig. 4. Typical SEM picture of a 100-μm-deep hybrid 1-D-PC without bumps, having design values $P = 4$ μm and $D = 69.5\%$, etched using the etching current profile reported in Fig. 3. Two magnifications of the top and the bottom of the etched structure, showing the high uniformity in both the horizontal and vertical directions, are also reported.

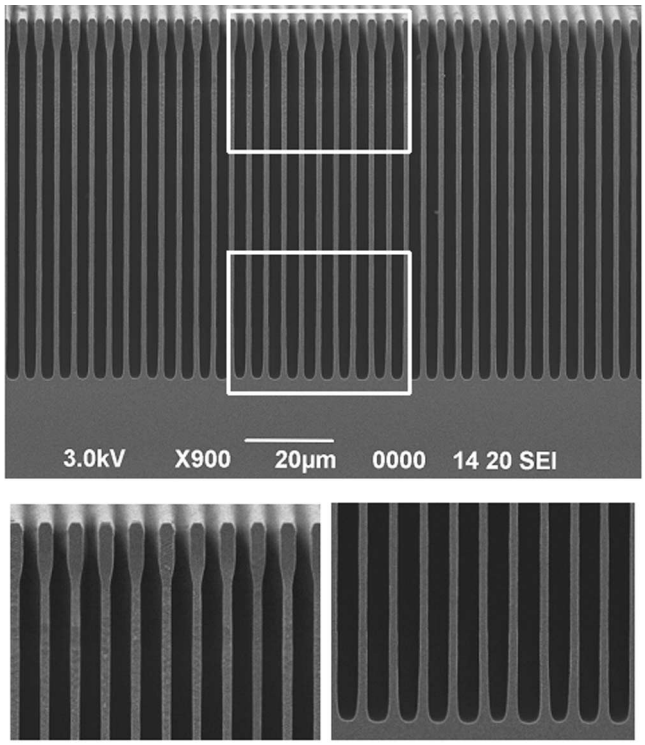

Fig. 5. Typical SEM picture of a 100-μm-deep hybrid 1-D-PC with 5-μm-long and 2-μm-thick bumps, having design values $P = 4$ μm and $D = 69.5\%$, obtained by using the etching current profile reported in Fig. 3. Magnifications of the top (with a detail of the bumps) and the bottom parts of the etched structure are also reported.

structure), for 100-μm-deep trenches. To further reduce stiction problems during the drying step, bumps can be used to diminish the surface contact area, and in turn, the attracting force F between silicon planes [21]. In our case, bumps were fabricated by increasing the thickness of silicon walls from 1.22 to 2 μm, for a length of 5 μm from the top. The bump length was chosen to obtain better mechanical stability of the structure during the drying process, without affecting the optical section, and in turn, the characteristics of PCs.

Bump fabrication was performed by using initially an etching current of 24.06 mA ($D = 50\%$) for 180 s, as reported in Fig. 3 (dotted line). Reducing the etching current at the beginning of the process increases the thickness of silicon walls at the top of the etched structure. Moreover, once bumps have been formed, the design specification can be matched by properly increasing the etching current to get a constant porosity value of 69.5% for the remaining part of the structure, as shown in Fig. 3. In order to understand the effect of bumps in reducing stiction, the critical length $l_{\rm crit}$ for the adhesion of a clamped-free cantilever in the final state of the drying process can be taken into account: $l_{\rm crit} = [(3/16)(Ed_{\rm Si}^3 d^2)/(\gamma_{\rm la}\cos\theta_{\rm c})]^{1/4}$, where $E = 150$ GPa is the Young's modulus of crystalline silicon, $d_{\rm Si}$ is the walls' thickness, d is half of the distance between adjacent walls, $\gamma_{\rm la}$ is the surface tension of the liquid–air interface, and $\theta_{\rm c}$ is the contact angle. For 100-μm-deep silicon walls that have a constant thickness of 1.22 μm separated by air gaps of 2.78 μm and that are filled with pentane ($\gamma_{\rm la} = 15.48$ mJ/m^2 and $\theta_{\rm c} = 20^\circ$), the critical length is about 50 μm. This means that the stiction length between adjacent cantilevers is about $l_{\rm stict} = 100$ μm – $l_{\rm crit} = 50$ μm. The attracting force F is proportional to $A/d = wl_{\rm stict}/d \cong 36w$, once a stiction width w is given. On the other hand, in the case of bumps at the top of the silicon walls, the stiction length $l_{\rm stict}$ is fixed to a value of 5 μm by the bump length, whereas the cantilever at the bump section is 2 μm thick, as well as the air gap. In this case, the attracting force F becomes proportional to $A/d = 2.5w$, which is over ten times lower than in the case without bumps for the same width w.

A typical result is reported in Fig. 5, which shows an SEM cross section of a 1-D-PC about 100 μm deep with 5-μm-long bumps at the top, along with two magnifications of the top and bottom part of the structure. The figure shows the high uniformity, for both the horizontal and vertical directions, of the etched structure.

Some samples were cut into two facing sections so that one half could be used as the reference while the other was oxidized, in order to analyze the changes induced in the optical characteristics of the structure by silicon dioxide thin layers. Rapid thermal oxidation (RTO) was performed at 1100 °C in O_2 atmosphere for different times in order to grow silicon dioxide layers of different thicknesses. According to the Deal–Groove model [22], oxide thicknesses of 24, 43, and 69 nm were grown using oxidation times of 200, 600, and 1800 s, respectively. For each oxidation time, the thickness of the grown oxide layer was experimentally measured on a reference sample, consisting

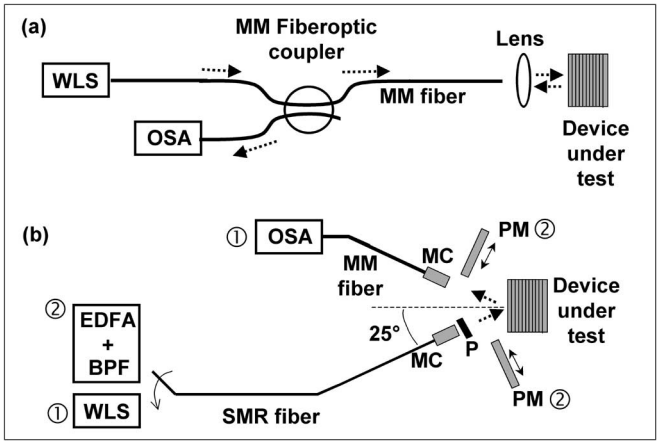

Fig. 6. Optical setup for reflectivity measurements. (a) Configuration for orthogonal incidence. (b) Configuration for 25° incidence: ① scheme for spectral reflectivity; ② scheme for absolute reflectivity. WLS: white light source; OSA: optical spectrum analyzer; MM: multimode; PM: power-meter; P: polarizer; MC: microcollimator; EDFA: erbium-doped fiber amplifier; BPF: bandpass optical filter.

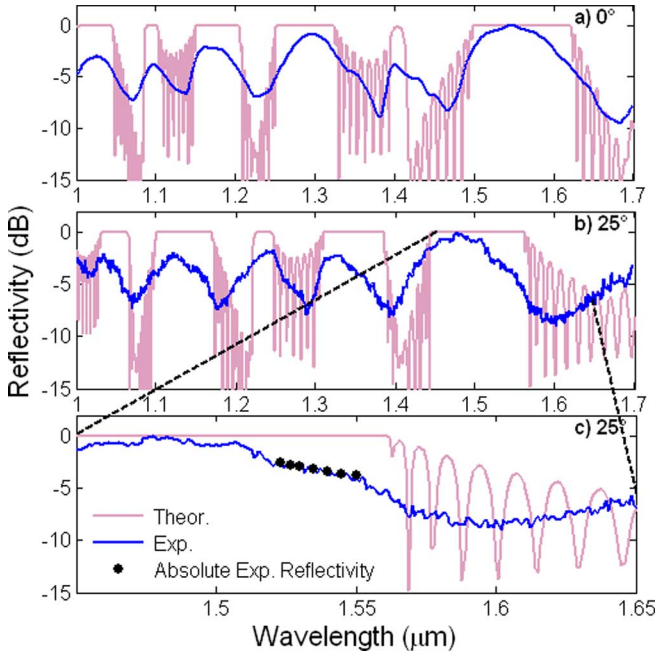

Fig. 7. Comparison between measured and calculated reflectivity at orthogonal and 25° incidence, and absolute reflectivity data. (a) Orthogonal incidence; black trace (blue online): experimental data of wideband normalized reflectivity; gray trace (pink online): calculated reflectivity, best fitted to experimental data with the design values $P = 4\ \mu$m and $D = 69.5\%$. (b) 25° incidence; black trace (blue online): experimental data of wideband normalized reflectivity; gray trace (pink online): calculated reflectivity for the TE mode, best fitted to experimental data with the design values $P = 4\ \mu$m, $D = 69.5\%$, and 25° incidence. (c) Zoom of the traces of (b) in the range 1.45–1.65 μm. Large black dots correspond to absolute values of experimental reflectivity at 25°. Results reported were all collected on the same sample of silicon 1-D-PC.

in a bare silicon die oxidized with the 1-D-PC, using a stylus microprofilometer.

III. Theoretical Calculations and Experimental Results for Spectral Reflectivity

We performed experimental measurements of spectral reflectivity on various samples of fabricated 1-D hybrid quarter-wavelength silicon microstructures and tested, in particular, devices that were subjected to thermal oxidation.

Changes in the optical characteristics of oxidized hybrid PCs are to be expected, with respect to nonoxidized 1-D-PC, due to the variation of the crystal structure. In fact, as the thermal oxidation of silicon results in consuming a silicon thickness equal to 44% of the grown oxide (the remaining 56% of the oxide grows outside in the air), the thickness of silicon walls and the air gap width are reduced as the oxide layer increases. While other complex and more expensive deposition techniques, such as CVD or sputtering, can be used to deposit dielectric layers, thermal oxidation of silicon has the advantage of having a better growth isotropy, especially for narrow, deep trenches.

Initially, for a more complete optical characterization of the fabricated devices, with respect to our previously published papers [5], [6], we investigated the optical properties of a reference sample with bumps by measuring not only the relative spectral reflectivity in the wavelength range of 1.0–1.7 μm but also the absolute reflectivity at specific wavelengths around 1.55 μm.

For the measurement of the spectral reflectivity at orthogonal incidence, we used the instrumental configuration reported in Fig. 6(a). White light radiation was shone onto the device by means of a multimode fiber-optic 50% coupler, which also carried the reflected light back to the optical spectrum analyzer (OSA) [5]. A spherical lens was used to compensate for the output divergence of the optical fiber and an angled termination for the fiber was employed to minimize reflections at the glass–air interface. In Fig. 7(a), we compare the experimental spectrum obtained with orthogonal incidence on a sample with bumps, designed with period $P = 4\ \mu$m and porosity $D = 69.5\%$, to the calculated spectrum best-fitted with the nominal parameters. Theoretical reflectivity spectra of ideal 1-D-PCs were calculated by means of the characteristic matrix method [23], using a wavelength-dependent complex refractive index for silicon [24] and a constant real value $n_{\mathrm{ox}} = 1.44$ for silicon dioxide. Experimental data of wideband spectral reflectivity have been plotted in all figures as normalized reflectivity, with respect to the peak output power, for an easier comparison with the calculated spectra. The theoretical position of the gaps is confirmed by the experimental data. For completeness, a numerical Monte Carlo analysis could also be performed, as explained in [6], for better fitting mainly with regard to the extinction ratio between reflectivity maxima and minima, but it was not significant for the purpose of this paper.

Since an absolute measurement of reflectivity at normal incidence is quite ambiguous because optical losses in that setup can only be roughly estimated, the absolute reflectivity of the sample was evaluated at an incidence angle of 25°, with the instrumental configuration reported in Fig. 6(b). Radiation was shone at an angle of 25° with respect to the orthogonal direction in the horizontal plane using a microcollimator with a single-mode fiber pigtail [single-mode reduced-core (SMR) fiber 9/125]. The selected microcollimator provided, at $\lambda = 1.55\ \mu$m,

an approximately 50-μm-diameter collimated spot at a working distance of 2.3 cm so that partialization on the front facet of the device was avoided. A sheet linear polarizer was placed at the collimator output to obtain linearly polarized TE light and the reflected radiation was collected at the Fresnel angle. The wideband reflectivity spectrum was attained by using the white light source [Fig. 6(b), ①] and coupling the radiation reflected by the silicon device into a multimode fiber pigtail (with a large area collimator) used for feeding the OSA. Results of this measurement on the same sample of Fig. 7(a) are shown in Fig. 7(b). For comparison, we are also reporting the calculated spectrum, in agreement with the experimentally detected wideband spectrum. The lower SNR of the spectrum collected at 25° with respect to the SNR typically obtained with orthogonal measurements is due to the low coupling efficiency of the available white light source into a single-mode optical fiber.

For the absolute measurement, we used amplified spontaneous emission from an erbium-doped fiber amplifier (EDFA) as a light source followed by a tunable optical bandpass filter with a 1 nm bandwidth, connected to the fiber pigtail of the microcollimator. With this configuration [Fig. 6(b), ②], we were able to collect the absolute values of reflected power by means of a large-area optical power-meter. In this case, we first tuned the optical filter to the selected wavelength by monitoring the output with the OSA, and then, with the power-meter, we measured the output power from the microcollimator and the reflected power from the silicon device. Absolute reflectivity was thus calculated as the ratio between these measured values, taken at each wavelength. Fig. 7(c), which contains a zoom of the region between 1.45 and 1.65 μm, illustrates the values of absolute reflectivity superposed and in perfect agreement with the experimentally detected, normalized wideband spectrum. From Fig. 7(c), we can therefore infer that the reflectivity peak, experimentally recorded at $\lambda = 1.48$ μm for a 25° incidence, actually assumes a value close to 0 dB, not only confirming the presence of a bandgap but also suggesting that the material exhibits negligible losses, at least at the reflectivity peak.

We also performed measurements of spectral reflectivity at orthogonal incidence, with the optical setup already described, on thermally oxidized devices. In these cases, we were mainly interested in the experimental verification of the bandgap tunability, so we compared the results of reflectivity measurements performed on the reference as well as on the oxidized section with a point-to-point correspondence. In Fig. 8(a), experimentally detected reflectivity spectra on the reference sample are compared to the calculated results, whereas in Fig. 8(b), experimental data relative to the oxidized section, with $t_{ox} = 200$ s, are superposed to the calculated results obtained with $d_{ox} = 24$ nm. Similarly, Fig. 9 shows the results relative to the second oxidation time $t_{ox} = 600$ s, compared to the calculated spectra obtained with an oxide thickness of $d_{ox} = 43$ nm, as experimentally measured. For an even more accurate comparison, in one case, we measured the reflectivity spectrum of the same sample, before and after a thermal oxidation of 1800 s, corresponding to a calculated and measured oxide layer of 69 nm. As for the previous examples, in Fig. 10, experimentally collected data are compared to the calculated results obtained by considering an oxide layer of 69 nm, as measured. In all cases, a good agreement between calculated spectra and experimental data was observed. Data in Figs. 8–10 demonstrate the good performances of the 1-D-PC fabrication process in terms of reproducibility since similar optical properties were exhibited by different reference samples and in terms of accuracy since the experimental data were in agreement with the theoretically calculated behavior.

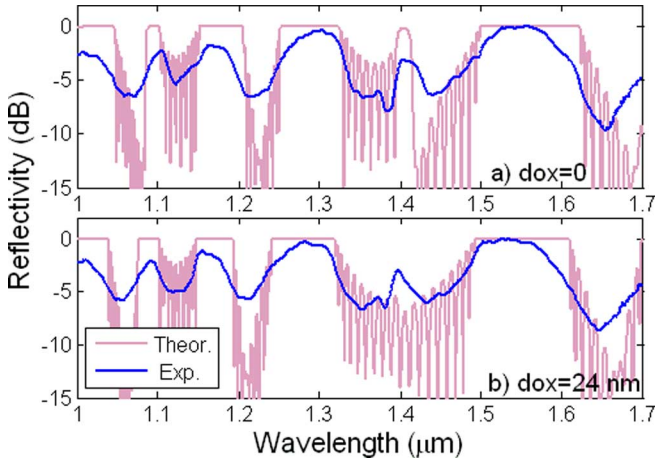

Fig. 8. Comparison between measured and calculated reflectivity for orthogonal incidence on oxidized device. (a) Reference sample; black trace (blue online): experimental data of wideband normalized reflectivity; gray trace (pink online): calculated reflectivity, best fitted to experimental data with the design values $P = 4$ μm and $D = 69.5\%$. (b) Oxidized sample; black trace (blue online): experimental data of wideband normalized reflectivity collected on the sample subject to thermal oxidation for 200 s; gray trace (pink online): calculated reflectivity, best fitted to experimental data with the design values and with oxide thickness $d_{ox} = 24$ nm, corresponding to the experimentally grown value.

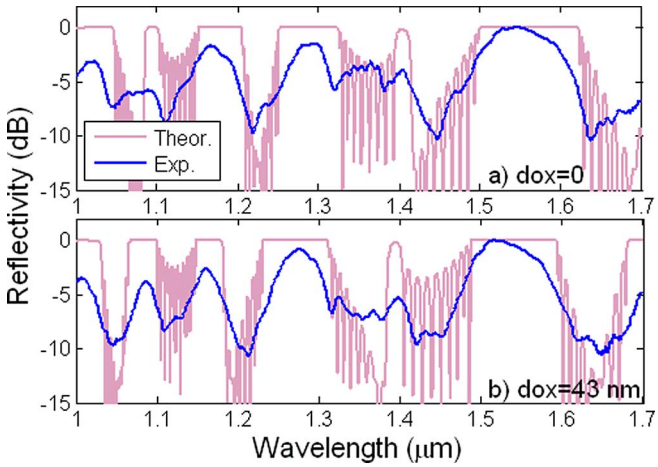

Fig. 9. Comparison between measured and calculated reflectivity for orthogonal incidence on oxidized device. (a) Reference sample; black trace (blue online): experimental data of wideband normalized reflectivity; gray trace (pink online): calculated reflectivity, best fitted to experimental data with the design values $P = 4$ μm and $D = 69.5\%$. (b) Oxidized sample; black trace (blue online): experimental data of wideband normalized reflectivity collected on the sample subject to thermal oxidation for 600 s; gray trace (pink online): calculated reflectivity, best fitted to experimental data with the design values and with oxide thickness $d_{ox} = 43$ nm, corresponding to the experimentally grown value.

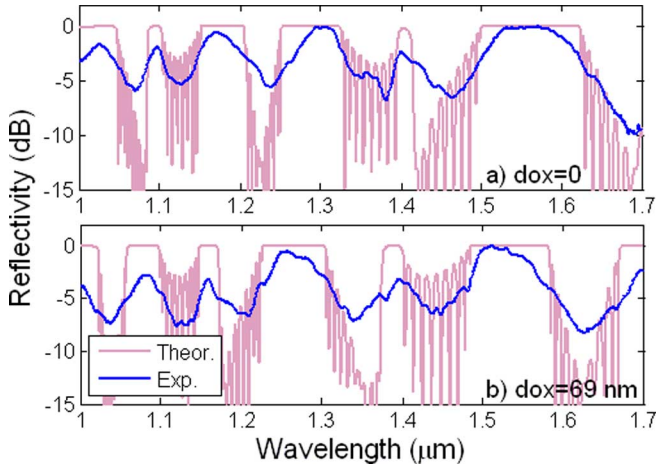

Fig. 10. Comparison between measured and calculated reflectivity for orthogonal incidence on oxidized device. (a) Reference sample; black trace (blue online): experimental data of wideband normalized reflectivity; gray trace (pink online): calculated reflectivity, best fitted to experimental data with the design values $P = 4$ μm and $D = 69.5\%$. (b) Sample after oxidation; black trace (blue online): experimental data of wideband normalized reflectivity collected on the same sample after thermal oxidation for 1800 s; gray trace (pink online): calculated reflectivity, best fitted to experimental data with the design values and with oxide thickness $d_{\rm ox} = 69$ nm, corresponding to the experimentally grown value.

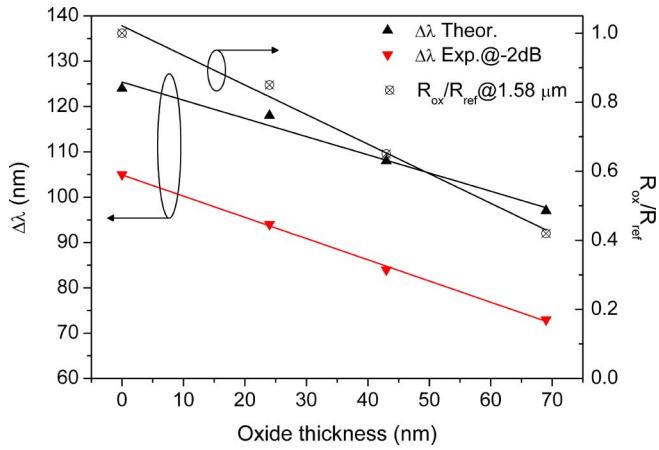

Fig. 11. Calculated value of the width $\Delta\lambda$ and experimental width at –2 dB of the bandgap centered at 1.55 μm (the ninth order) as a function of the oxide thickness. The experimentally detected ratio $R_{\rm ox}/R_{\rm ref}$ at 1.58 μm for each tested sample is also shown. Linear best fittings have also been added.

Figs. 8(b), 9(b), and 10(b) show that, as the oxide layer increases, the spectrum shifts toward shorter wavelength (blue-shift), with a line-shape only slightly changed for thin oxide thicknesses, but with more significant changes in the case of thick oxide layers. In particular, the bandgap around 1.55 μm becomes narrower as the oxide increases, at least for the measured oxide thicknesses. For a direct comparison among the effects induced by the oxide, in Fig. 11, we are reporting the calculated width $\Delta\lambda$ and the experimental width at -2 dB of the bandgap centered at 1.55 μm (the ninth order) as a function of the oxide thickness: the experimental trend follows the theoretically expected behavior. Also shown is the experimental ratio $R_{\rm ox}/R_{\rm ref}$ at $\lambda = 1.58$ μm, where $R_{\rm ox}$ and $R_{\rm ref}$ are the reflectivities obtained, respectively, on the oxidized and on the reference sample. Linear best fittings of the data have also been added.

IV. Conclusion

We have demonstrated that the ECM represents a very powerful technique for the fabrication of silicon-based bandgap materials for optical applications.

In principle, economically viable devices could be manufactured with this process. Our findings could give a contribution to the growing field of silicon photonics, which is also largely investigated by important companies. The material that we have designed, fabricated, and tested could be considered as a 3-D platform that can be tailored for different purposes to obtain specific optical devices. An interesting feature could be the possibility to realize with the same process vertical structures with periodicity along one and two dimensions on the same substrate. This platform also seems interesting for realizing sensors: the experimental observations performed on the oxidized samples indicate that we are able to optically monitor the growth of nanometer-thick layers of a material with a refractive index around 1.5.

Further work will be devoted to the exploitation of the presented fabrication process and design approach for the realization of specific optical devices, such as resonant microcavities, and test structures with an increasing number of periods for transmission measurements, in order to get the information on the effective losses of the material outside the bandgaps. Numerical studies including a more detailed model of the optical beam and of its propagation in the material, e.g., taking into account the effects of the beam divergence, would probably be helpful for better fitting the experimental data.

Acknowledgment

The authors wish to thank Prof. V. Annovazzi-Lodi and Prof. A. Diligenti for fruitful discussions. S. Merlo would like to thank G. Maida for assistance with the measurements.

References

[1] B. Jalali and S. Fathpour, "Silicon photonics," *J. Lightw. Technol.*, vol. 24, no. 12, pp. 4600–4615, Dec. 2006.
[2] A. Birner, R. B. Wehrspohn, U. M. Gösele, and K. Busch, "Silicon-based photonic crystals," *Adv. Mater.*, vol. 13, no. 6, pp. 377–388, Mar. 2001.
[3] A. Lipson and E. M. Yeatman, "A 1-D photonic band gap tunable optical filter in (110) silicon," *J. Microelectromech. Syst.*, vol. 16, no. 3, pp. 521–527, Jun. 2007.
[4] V. A. Tolmacheva, E. V. Astrova, J. A. Pilyugina, T. S. Perova, R. A. Moore, and J. K. Vij, "1D photonic crystal fabricated by wet etching of silicon," *Opt. Mater.*, vol. 27, no. 5, pp. 831–835, Feb. 2005.
[5] G. Barillaro, A. Diligenti, M. Benedetti, and S. Merlo, "Silicon micromachined periodic structures for optical applications at $\lambda = 1.55$ μm," *Appl. Phys. Lett.*, vol. 89, pp. 151110-1–151110-3, 2006.
[6] G. Barillaro, V. Annovazzi-Lodi, M. Benedetti, and S. Merlo, "Reflection properties of hybrid quarter-wavelength silicon microstructures," *Appl. Phys. Lett.*, vol. 90, pp. 121110-1–121110-3, 2007.
[7] H. Krause, W. Mönch, and H. Zappe, "Replicated, high-aspect-ratio micro-optical components fabricated from inorganic sol gel materials," *Appl. Opt.*, vol. 45, no. 20, pp. 4843–4849, Jul. 2006.
[8] K. B. Mogensen, F. Eriksson, O. Gustafsson, R. P. H. Nikolajsen, and J. P. Kutter, "Pure-silica optical waveguides, fiber couplers, and

high-aspect ratio submicrometer channels for electrokinetic separation devices," *Electrophoresis*, vol. 25, pp. 3788–3795, 2004.

[9] M. W. Pruessner, W. S. Rabinovich, T. H. Stievater, D. Park, and J. W. Baldwin, "Cryogenic etch process development for profile control of high aspect-ratio submicron silicon trenches," *J. Vac. Sci. Technol. B*, vol. 25, no. 1, pp. 21–28, Jan./Feb. 2007.

[10] G. Barillaro, A. Nannini, and F. Pieri, "Dimensional constraints on high aspect ratio silicon microstructures fabricated by HF photoelectrochemical etching," *J. Electrochem. Soc.*, vol. 149, pp. C180–C185, 2002.

[11] G. Barillaro, A. Nannini, and M. Piotto, "Electrochemical etching in HF solution for silicon micromachining," *Sens. Actuators A*, vol. 102, pp. 195–201, 2002.

[12] G. Barillaro, P. Bruschi, A. Diligenti, and A. Nannini, "Fabrication of regular silicon microstructures by photo-electrochemical etching of silicon," *Phys. Status Solidi C*, vol. 2, no. 9, pp. 3198–3202, 2005.

[13] V. Lehmann and H. Föll, "Formation mechanism and properties of electrochemically etched trenches in n-type silicon," *J. Electrochem. Soc.*, vol. 137, pp. 653–658, 1990.

[14] V. Lehmann, "The physics of macropore formation in low-doped n-type silicon," *J. Electrochem. Soc.*, vol. 140, pp. 2836–2843, 1993.

[15] V. Lehmann and U. Grüning, "The limits of macropore array fabrication," *Thin Solid Films*, vol. 297, pp. 13–17, 1997.

[16] G. Barillaro, A. Diligenti, A. Nannini, and G. Pennelli, "A thick silicon dioxide fabrication process based on electrochemical trenching of silicon," *Sens. Actuators A*, vol. 107, pp. 279–284, 2003.

[17] G. Barillaro, F. D'angelo, G. Pennelli, and F. Pieri, "Fabrication of self-aligned gated silicon microtip array using electrochemical silicon etching," *Phys. Status Solidi A, Appl. Mater. Sci.*, vol. 202, no. 8, pp. 1427–1431, 2005.

[18] G. Barillaro, A. Nannini, and M. Piotto, "Electrochemical fabrication of buried folded microchannels into silicon substrates," *Phys. Status Solidi. A, Appl. Mater. Sci.*, vol. 204, no. 5, pp. 1464–1468, 2007.

[19] H. Ohji, S. Izuo, P. J. French, and K. Tsutsumi, "Macroporous-based micromachining on full wafers," *Sens. Actuators A*, vol. 92, pp. 384–387, 2001.

[20] G. Barillaro and F. Pieri, "A self-consistent theoretical model for macropore growth in n-type silicon," *J. Appl. Phys.*, vol. 97, no. 11, pp. 1–3, 2005.

[21] N. Tas, T. Sonnenberg, H. Jansen, R. Legtenberg, and M. Elwenspoek, "Stiction in surface micromachining," *J. Micromech. Microeng.*, vol. 6, pp. 385–397, 1996.

[22] J. D. Plummer, M. D. Deal, and P. B. Griffin, *Silicon VLSI Technology—Fundamentals, Practice and Modeling*. Upper Saddle River, NJ: Prentice-Hall, 2000.

[23] H. A. Macleod, *Thin-Film Optical Filters*. London, U.K.: Adam Hilger, 1969.

[24] E. D. Palik and R. T. Holm, *Handbook of Optical Constants of Solids*, D. Palik, ed. New York: Academic, 1998.

Giuseppe Barillaro was born in Melito di Porto Salvo, Italy, in 1973. He received a graduate degree in electronic engineering and the Ph.D. degree in information engineering from the Università di Pisa, Pisa, Italy, in 1998 and 2002, respectively.

From November 2002 to November 2005, he was a Postdoctoral Research Fellow in the Dipartimento di Ingegneria dell'Informazione: Elettronica, Informatica, Telecomunicazioni, Università di Pisa, where, since December 2005, he has been a permanent Researcher. His current research interests include design, modeling, fabrication, and characterization of new materials and devices with applications ranging from photonics to microelectronics, and from microelectromechanical systems (MEMS) to biomedics. He is the author of more than 25 papers and holds an international patent.

Sabina Merlo (M'01–SM'05) was born in Pavia, Italy, in 1962. She received a graduate degree and the Ph.D. degree in electronic engineering from the Università degli Studi di Pavia, Pavia, in 1987 and 1991, respectively, and the M.S.E. degree in bioengineering from the University of Washington, Seattle, in 1989.

In 1993, she became an Assistant Professor in the Dipartimento di Elettronica, Università degli Studi di Pavia, where, in 2001, she became an Associate Professor. Her current research interests include microelectromechanical systems (MEMS), microoptoelectromechanical systems (MOEMS), chaos in lasers, laser interferometry, fiber-optic passive components, and sensors. She holds three patents and is the author of more than 60 papers.

Dr. Merlo is an Associate Editor of the IEEE/ASME JOURNAL OF MICROELECTROMECHANICAL SYSTEMS. She is a member of the Electrical Italian Association (AEIT) and a Senior Member of the IEEE Lasers and Electro-Optics Society (LEOS). She was the recipient of a Rotary Foundation Graduate Scholarship for studying at the University of Washington, Seattle.

Lucanos Marsilio Strambini received a graduate degree in electronic engineering and the Ph.D. degree in information engineering from the Università di Pisa, Pisa, Italy, in 2002 and in 2007, respectively.

Since August 2007, he has been a Postdoctoral Fellow in the Dipartimento di Ingegneria dell'Informazione: Elettronica, Informatica, Telecomunicazioni, Università di Pisa. His current research interests include porous silicon applications and technologies, silicon and glass micromachining, solid-state sensors, microelectronics devices, and technologies.